Available online at www.sciencedirect.com

SCIENCE DIRECT®

Earth and Planetary Science Letters 232 (2005) 295–314

EPSL

www.elsevier.com/locate/epsl

Microstructure, texture and seismic anisotropy of the lithospheric mantle above a mantle plume: Insights from the Labait volcano xenoliths (Tanzania)

Alain Vauchez[a,*], Florence Dineur[a], Roberta Rudnick[b,1]

[a]*Laboratoire de Tectonophysique, ISTEEM- UMR 5568, Université de Montpellier 2 and CNRS, Place E, Bataillon F-34095 Montpellier cedex 05, France*
[b]*Department of Geology, University of Maryland, College Park, Maryland 20742, USA*

Received 9 July 2004; received in revised form 3 January 2005; accepted 19 January 2005
Available online 17 March 2005
Editor: R.D. van der Hilst

Abstract

The impact of a mantle plume at the base of the Tanzania craton has modified the composition and seismic velocity of the lithospheric mantle. Lavas erupted by the Labait volcano have sampled the perturbed mantle from the lithosphere–asthenosphere boundary (>140 km) to the spinel-peridotite domain (<70 km). We have studied the microstructure, texture and seismic anisotropy of a set of xenoliths spanning these depths to investigate the effects of plume activity on the fabric and seismic properties of the lithospheric mantle. The microstructure changes with depth: first the grain-size increases significantly, and then nucleation recrystallization occurs. The deepest samples display a recrystallized equidimensional matrix embedding relicts of deformed paleoclasts. The crystallographic preferred orientation (CPO) of olivine remains clear and even tends to increase with depth. In most samples, the observed CPO is consistent with dominant activation of the (010)[100] slip system. Samples from the base of the lithosphere display more unusual CPO, suggesting increasing activity on the (010)[001] slip system. Nucleation recrystallization does not appear to modify the pre-existing CPO, since neoblasts have a crystallographic orientation close to the parent grain orientation. Seismic properties remain similar over the whole section. In particular, no weakening of the seismic anisotropy is observed with depth, either for the P azimuthal or for the S polarization anisotropies. These results are consistent with previous seismological observations suggesting a coherent seismic anisotropy over the entire thickness of the Tanzania cratonic lithosphere. Our data thus provide new constraints for interpreting shear wave splitting measurements in East Africa, and support a model of perturbed lithosphere characterized by seismic signatures transitional between the "normal" lithosphere (for seismic anisotropy) and asthenosphere (for seismic velocities).
Published by Elsevier B.V.

Keywords: cratonic lithosphere; mantle plume; xenoliths; microstructure; crystallographic preferred orientation; seismic anisotropy; Tanzania; Labait volcano

* Corresponding author. Tel.: +33 467 14 38 95; fax: +33 467 14 36 03.
E-mail addresses: vauchez@dstu.univ-montp2.fr (A. Vauchez), rudnick@geol.umd.edu (R. Rudnick).
[1] Tel.: +1 301 405 1311; fax: +1 301 314 9661.

0012-821X/$ - see front matter. Published by Elsevier B.V.
doi:10.1016/j.epsl.2005.01.024

1. Introduction

Data from seismology (e.g., [1–3]), geochemistry (e.g., [4,5]) and numerical modeling (e.g., [6,7]) consistently suggest that cratonic lithosphere may remain stable over long periods of time. However, processes such as rifting or impingement of an upwelling mantle plume may trigger destabilization of the cratonic lithosphere. Beneath continental rifts or above a mantle plume, asthenosphere and lithosphere deeply interact. The lowermost lithosphere might be eroded through reheating (upward migration of the isotherms by thermal conduction) and through the thermo-mechanical action of small-scale convection cells (e.g., [8]). Moreover, magmas resulting from decompression melting of upwelling asthenosphere may percolate through the lithosphere, advecting heat and modifying its microstructure. As a consequence, seismic velocities of the mantle lithosphere are significantly reduced and its apparent thickness diminished, since the boundary between the asthenosphere and the seismic lithosphere can be equated with the transition between the seismically "fast" lithospheric domain and the abnormally "slow" underlying domain. However, relatively little is known about how the microstructure, texture and resulting seismic anisotropy of the thermally and chemically modified mantle lithosphere are affected by these processes. This is an important issue since: (1) determining lithospheric thickness based only on seismic velocity may lead to underestimates [9], and (2) the contribution of the lithospheric mantle to measured seismic anisotropy is a function of both the bulk anisotropy (which depends mostly on the crystallographic fabric of olivine) and the thickness of the lithospheric lid. An improved understanding of lithosphere–asthenosphere interactions and their effects on seismic properties will therefore aid in the interpretation of seismic anisotropy.

Mantle xenoliths brought to the surface by the Labait volcano (Fig. 1) provide a unique opportunity to study the interaction between an active rift and a cratonic lithosphere. The Labait area is the only area in East Africa where evidence of modification of the Tanzania craton by the eastern branch of the East African Rift is observed in both body wave (e.g., [10,11]) and surface wave data [3]. Recent geochemical [12,26] and seismological (e.g., [10]) studies

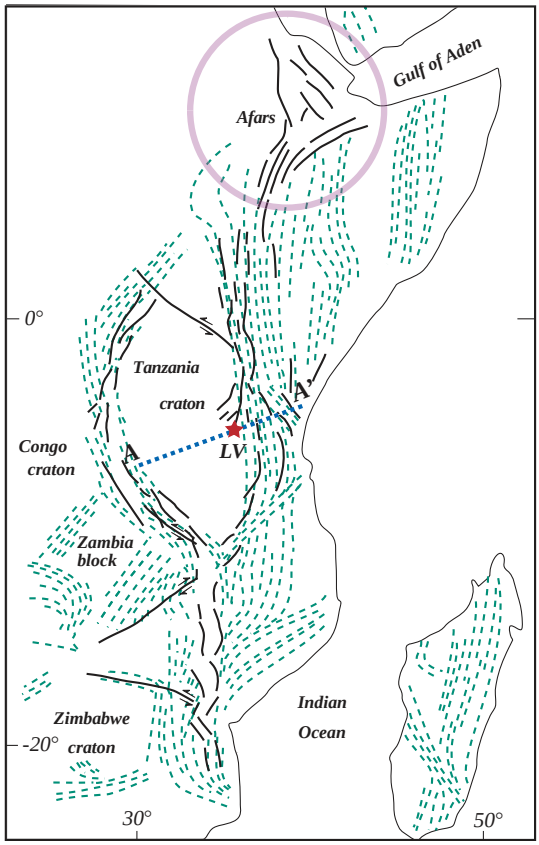

Fig. 1. Sketch map of East Africa showing location of the main cratonic blocks, the mobile belts surrounding the cratons (grey, stippled lines), the main faults related to the East African Rift (black, continuous lines) and the possible zones of impact of the plumes at the base of the lithosphere (gray circles). The star labelled LV marks the location of the Labait volcano. Line labelled AA′ marks the location of the vertical cross-section shown on Fig. 2.

in Northern Tanzania suggest that the base of the lithosphere has been modified by the plume, and that the asthenosphere–lithosphere transition is gradational (Fig. 2). A similar progressive modification of the continental lithosphere (asthenospherization) by the action of heat, partial melting and percolating fluids was proposed by Vauchez and Garrido [9] based on a combined geochemical and petrophysical study of peridotites across a melting front fossilized in the Ronda massif (Spain). In this paper, we describe the microstructures and textures of the Labait peridotite xenoliths and compute their seismic properties. These xenoliths equilibrated at depths ranging from <70 km (spinel peridotites facies) to ~140 km and at temperatures of <1000 °C to >1400 °C (Fig. 2). Although it

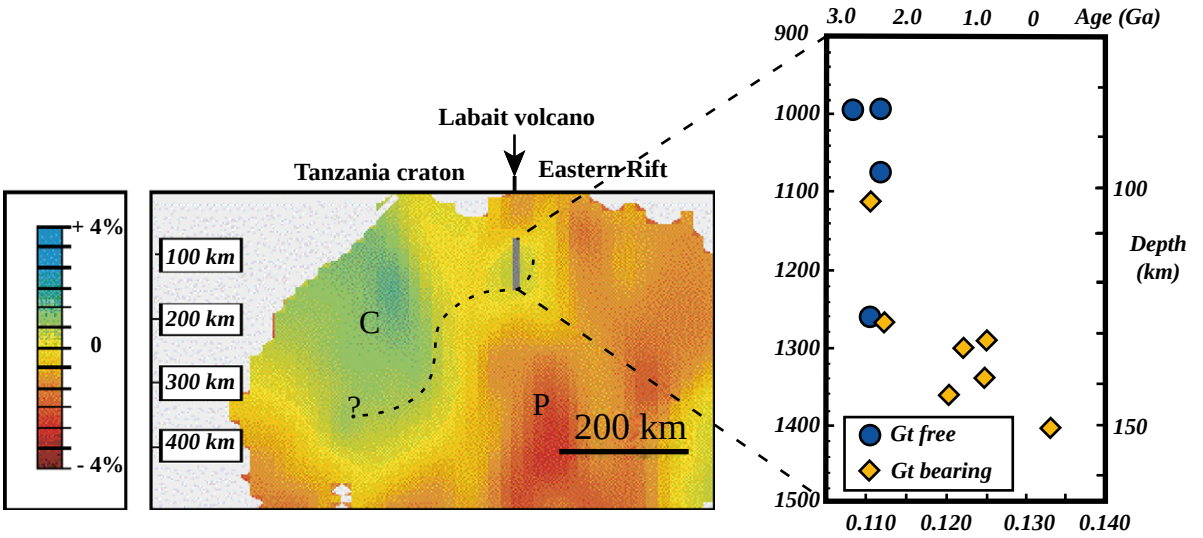

Fig. 2. Location of the mantle section sampled by the lavas of the Labait volcano on a vertical section across the S velocity model by Ritsema et al. [2] "Cold" colors indicate higher-than-average velocities within the Tanzania craton (C) and "hot" colors indicate lower-than-average velocities corresponding to the plume (P). The stippled line marks the possible base of the lithosphere, which is poorly constrained beneath the Tanzania craton [2]. The diagram on the right shows the change in $^{187}Os/^{188}Os$ [26] with depth (lower *X*-axis). Equilibration temperatures are shown on the left *Y*-axis, whereas Re-depletion model ages are shown on the upper *X*-axis. *P*–*T* estimates are from [12].

is uncertain to what extent the xenoliths are representative, the large, rather exceptional, span of equilibration depths of the xenoliths provides important information on the evolution of the microstructure, texture and seismic properties with depth in the lithosphere, including its lowermost boundary with the asthenosphere. Thus, we can evaluate how impingement of a mantle plume may affect the fabric and seismic properties of cratonic mantle, and compare splitting measurements performed in East Africa to the seismic properties of lithospheric mantle.

2. The East African Rift and the Labait volcano

The East African Rift (Fig. 1) is one of the main active continental rifts on Earth. It developed during the last 4 My [13,14] in a lithosphere stabilized since the Neoproterozoic. Recent tomographic models (e.g., [15]) suggest that the whole East African Rift system (Afar and East African Rift) might be related to a single super-plume extending from the core–mantle boundary beneath the southeastern Atlantic Ocean into the upper mantle beneath East Africa. On the other hand, Sr, Nd an Pb isotope evidences from Kenyan and Afar Rift basalts [16] suggest the impact of two mantle plumes at the base of the lithosphere: one beneath the Afar and the other beneath the Tanzania craton (Fig. 1). Evidence for a mantle plume beneath the Tanzania cratonic lithosphere was obtained using body-waves [10,17] and surface-waves velocity models [3,18]. The negative seismic velocity anomaly beneath the Tanzania craton is significantly stronger than the anomaly usually recorded beneath other cratonic domains, suggesting that an upwelling mantle plume heated the sublithospheric mantle [3]. The presence of deep, hot mantle is also supported by a downward deflection of the 440 km-discontinuity [10].

The first manifestations of plume activity in East Africa, based on the timing of the volcanism, likely occurred 50–30 My ago. Then rifting propagated from North to South [13,16,51] during the Cenozoic. The initial rifting was characterized by normal and transcurrent faulting (transtension) coupled with reactivation of the Proterozoic tectonic fabric [19,20]. This, together with shear-wave splitting, recorded both inside and outside the rift [21–24], suggests that the structure of the EAR results from interaction between a mantle plume and anisotropic continental litho-

sphere containing crystallographic preferred orientations of olivine inherited from Proterozoic orogenies [20,25].

The Labait volcano erupted in the Quaternary [5], thus, xenoliths entrained in these lavas sample the present-day mantle beneath the Tanzanian craton [12]. Re–Os systematics and whole-rock chemistry suggest that most of the mantle section sampled by the Labait volcano formed during the Archean [26] and subsequently remained stable until the plume/rift system developed and started to interact with the cratonic mantle. Lee and Rudnick [12] give a detailed description of the Labait xenoliths, together with their modal and chemical characteristics. Three quarters of the collected xenoliths are Fe-rich dunites and wehrlites and about a quarter are harzburgites and clinopyroxene-poor lherzolites. The latter group is further classified as spinel- or garnet-facies peridotites, based on either the presence of garnet or, in the absence of garnet, on the spinel and orthopyroxene chemistry and calculated equilibrium temperatures [12].

2.1. Pressure–temperature estimates

PT conditions of equilibrium for samples used in this study were calculated by Lee and Rudnick [12] using Brey and co-worker's formulation of the aluminum solubility in orthopyroxene coexisting with garnet barometer and the two-pyroxene thermometer [27]. Spinel-peridotites (<70 km deep) yield equilibrium temperatures around 1000 °C. Equilibration conditions in the range 3.7 GPa–1140 °C to 4.7 GPa–1460 °C were estimated for garnet-peridotites; these values fall near a geotherm corresponding to a surface heat flux of 50 mW/m^2 [12], significantly higher than the one inferred from surface heat flow (23–47 mW/m^2; [28,29]). Equilibrium temperatures of garnet peridotites are also 200–250 °C higher than those expected from the PREM for a "normal" lithosphere [12]. This abnormal thermal regime may result from the perturbation of the Tanzania cratonic lithosphere by the plume–rift system. Heating of the Tanzanian lithosphere in response to plume activity is also suggested by higher CaO contents in rims of some primary orthopyroxenes, and higher CaO and Al_2O_3 in pyroxenes from garnet coronas, suggesting that rims and coronas have recorded temperatures 100–200 °C higher than the cores. This heating event may have also caused garnet breakdown [12,30].

2.2. Microstructure

The microstructure of the Labait xenoliths correlates with temperature and depth. Spinel-peridotites (LB11, LB14) yield the lowest equilibrium temperatures (~990 °C) and have subequant to tabular olivine and pyroxene grains 2–6 mm in diameter (Fig. 3). Some of the largest crystals are elongated, with shape ratios in the range 1:2–1:4; their shape preferred orientation marks the foliation. These large crystals usually display undulose extinction and subgrain boundaries. Olivine grain boundaries show gentle curvatures suggesting limited grain boundary migration or partial recovery. Orthopyroxene frequently displays embayments filled with olivine, and small orthopyroxene crystals are included in olivine suggesting dissolution of orthopyroxene and crystallization of olivine.

The second type of microstructure is observed in the remaining garnet-free, chromite-bearing peridotites and in the garnet-peridotite that yields the lowest PT conditions (LB34, 3.7 GPa and 1115 °C; Fig. 4A). These coarse-grained samples have 5–15 mm diameter olivines and typically smaller (2–5 mm) orthopyroxenes. Primary clinopyroxene, when present, is a few millimeter large. Olivine and pyroxene crystals are subequant to slightly elongated and free of substructure; they are frequently poikiloblastic, including round

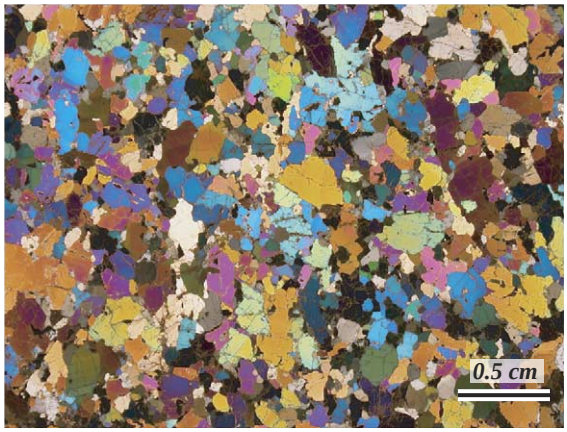

Fig. 3. Typical microstructure of spinel lherzolite (LB11). Detailed description in text. Crossed polarizers.

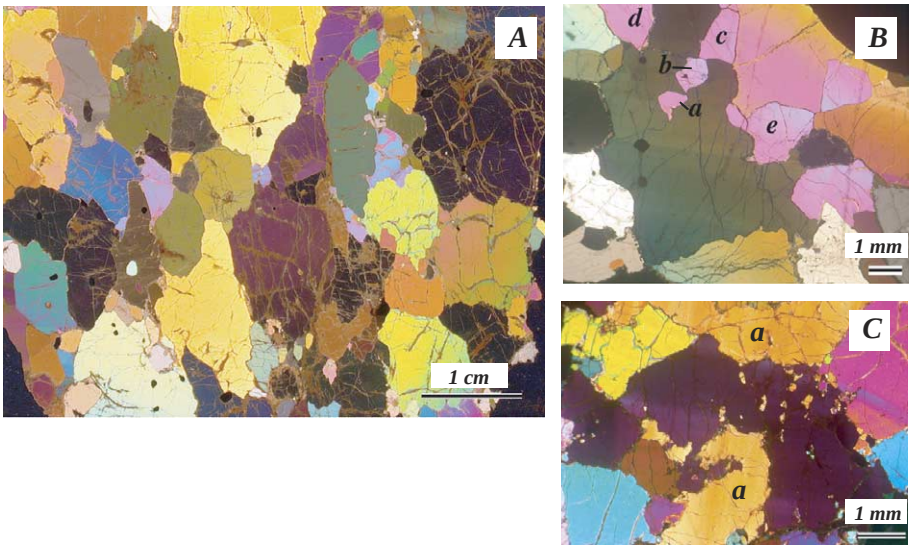

Fig. 4. Coarse-grained, "garnet-free" lherzolite (A, LB9), harzburgite (B, LB1) and garnet harzburgite (C, LB34). Olivine crystals are frequently >1 cm and display evidence of grain growth through grain boundary migration and bulging (B: grains a, b, c, d and e are domains from a single grain that either are still connected, revealing a complex grain boundary geometry, or have been recrystallized through bulging). Olivine in panel C shows nucleation recrystallization of grain a through bulging in an adjacent crystal. Crossed polarizers.

blebs of chromite and small crystals of orthopyroxene in olivine and of olivine in orthopyroxene. Olivine displays serrated grain boundaries and isolated remains of one crystal are often observed in a neighbor crystal (Fig. 4B,C). This suggests grain growth and limited nucleation recrystallization through bulging, i.e., large mobility of grain boundaries due to active diffusion. Some orthopyroxene crystals display embayments filled by olivine, suggesting dissolution coeval with olivine growth. The variable habit of orthopyroxene (either partially dissolved or poikiloblastic) may reflect two successive generations of orthopyroxene, with partially dissolved crystals representing the earliest generation.

At increasing equilibrium temperatures, garnet-peridotites evolve from the previously described coarse-granular microstructure towards a largely, to totally recrystallized, equigranular microstructure. Intermediate samples may still contain large olivine porphyroclasts, but also contain a significant proportion of neoblasts (Fig. 5). In contrast to the coarse-grained samples, the largest crystals of olivine in the recrystallized peridotites (which may be >1 cm) systematically display a well-developed substructure consisting of straight (100) subboundaries limiting relatively narrow subgrains. Recrystallized neoblasts first occur as patches of fine grains (100–200 μm) in high strain domains and along grain boundaries (Fig. 6), then progressively form a groundmass of equi-

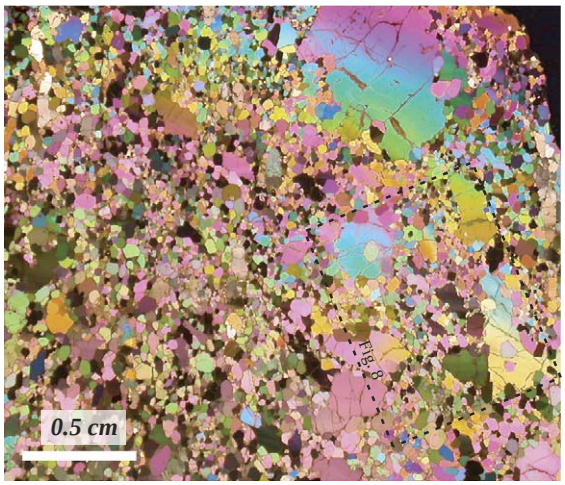

Fig. 5. Recrystallized Gt-harzburgite (KAT17) showing large paleoclasts of olivine embedded in a finer grained, recrystallized matrix. Paleoclasts show evidence of plastic deformation; they are surrounded by a fine-grained matrix of neoblasts. Recrystallized grains are 0.5–1 mm in size and many of them display a polygonal "subautomorphic" shape (Fig. 8 provides a close-up view of the area demarcated by the stippled square). Crossed polarizers.

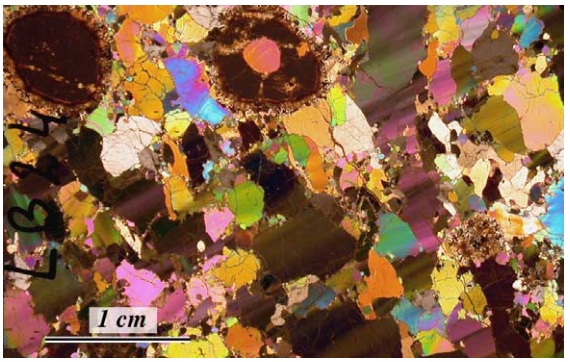

Fig. 6. Slightly recrystallized, coarse-grained Gt-harzburgite (LB24). Unusually large paleoclasts are elongated and display a well-developed substructure suggesting dislocation-flow. Incipient nucleation recrystallization occurs along grain boundaries. Crossed polarizers.

dimensional, strain-free olivine crystals embedding relicts of original grains characterized by their irregular shape and their substructure (Fig. 7). Neoblasts display evidence of high grain boundary mobility, spanning from equilibrated, 120° triple junctions at neoblast–neoblast contacts, to convex grain boundaries when in contact with relict crystals. The average size of neoblasts tends to increase with equilibrium temperature, reaching 300–500 μm in diameter in the deepest xenoliths. As observed by Lee and Rudnick [12], a second generation of olivine neoblasts is observed in recrystallized samples and becomes more frequent with increasing temperature and depth. These neoblasts (Fig. 8), impurity-free under the microscope, are significantly larger (≥500 μm) than the previous ones, and have a polygonal, frequently tabular shape ("subautomorphic" olivine, [31,32]). Their straight boundaries clearly penetrate the residual porphyroclasts, and even truncate neoblasts from the first generation, clearly demonstrating their late growth. In xenoliths equilibrated at the highest temperatures (LB45, LB50), limited recrystallization of orthopyroxene (fine-grained neoblasts are 30–50 μm) may be observed, as well as a few orthopyroxene subautomorphic neoblasts that, in some cases, truncate olivine subautomorphic grains. This suggests that a small amount of orthopyroxene either crystallized or nucleated at high temperature.

The olivine neoblasts in the high-temperature, recrystallized peridotites are remarkably similar to those produced experimentally during high-temperature annealing of previously strained olivine crystals or polycrystalline aggregates [33,34]. In these annealing experiments, both "normal" and subautomorphic neoblasts are formed through static recrystallization involving nucleation and growth. Nucleation recrystallization is mainly driven by differences in internal energy between adjacent grains, and involves grain boundary migration. Grain growth subsequent to recrystallization allows a

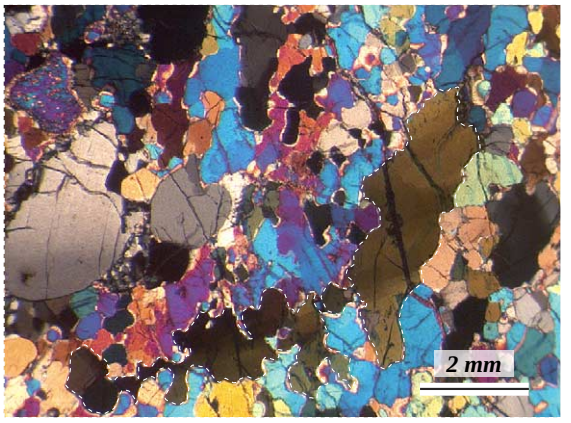

Fig. 7. Remnants of a paleoclast (outlined in white stippled line) in largely recrystallized Gt-harzburgite (KAT1). The size of the paleoclast and evidence of strained lattice suggest that this microstructure developed through nucleation recrystallization of a deformed, coarse-grained rock. Crossed polarizers.

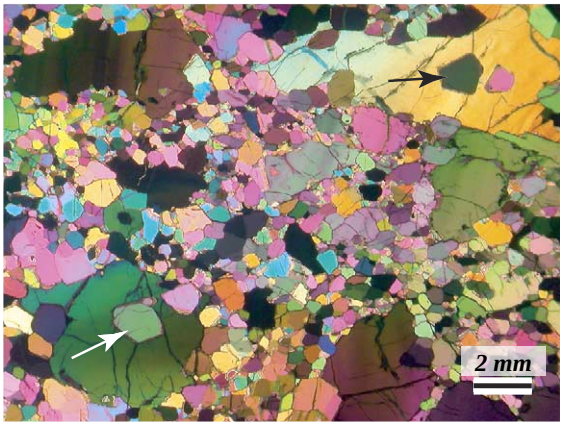

Fig. 8. Detail of Fig. 5 showing subautomorphic olivine neoblasts (arrows) within olivine paleoclasts of KAT17. The paleoclasts show evidence of lattice deformation; subautomorphic olivine neoblasts are free of substructure, polygonal in shape and may develop at the expense of either paleoclasts or neoblasts of the matrix. Crossed polarizers.

decrease of the surface energy and is usually accompanied by a polygonization of the grain boundaries. Fast growth of tabular, "subautomorphic" " crystals is favored by the presence of a fluid phase (e.g., [31,35]). This suggests that recrystallization in the Labait HT xenoliths was dominated by nucleation and growth, although a subsidiary participation of subgrain rotation recrystallization cannot be ruled out. The first generation of neoblasts is most likely related to the temperature increase due to the plume. Nucleation initiated in large, plastically deformed paleoblasts, as suggested by substructures observed in residual grains. The "subautomorphic" neoblasts may have developed later during magma (+xenoliths) upwelling. It remains uncertain whether recrystallization was static, like in Nermond's experiments [34], or triggered by a deformation of the base of the cratonic lithosphere due to rifting or to coupling with the flow of the plume head.

2.3. Texture

The crystallographic preferred orientations (CPO) of olivines and pyroxenes have been measured by indexation of Electron Back-Scattered Diffraction (EBSD) patterns using the JEOL JSM 5600 of the Laboratoire de Tectonophysique, Université de Montpellier II. EBSD patterns are generated by the interaction of a vertical incident electron beam with a carefully polished sample inclined at 70° with respect to horizontal. Diffraction patterns are projected onto a phosphor screen then captured by a low-light, high-resolution CCD camera. The image is then digitally processed and indexed in terms of mineral phase and crystal orientation using the CHANNEL+ software from HKL Technology. Measurements were performed on a grain-by-grain basis and in operator-controlled indexing mode in order to avoid pseudo-symmetry errors for olivine. Detailed CPO measurements of neoblast–paleoclasts systems in xenoliths recrystallized at high temperature were performed using orientation contrast imagery, which allows one to measure the crystallographic orientation of grains on the basis of their proximity to relict parent grains.

Fabric strength was computed using Bunge's *J*-index [36,37]. *J* is a dimensionless fabric strength index obtained by the integration of the density of the orientation distribution function (ODF) $f(g)$ at orientation g over the entire volume:

$$J = \int f(g)^2 \mathrm{d}g$$

where $\mathrm{d}g = \mathrm{d}\varphi_1 \mathrm{d}\phi \mathrm{d}\varphi_2 \sin\phi/\pi^2$ (φ_1, ϕ, φ_2 are the Euler angles) [36]. For a random distribution $J=1$ and for a single crystal (perfect CPO) J is infinite. Natural samples of mantle peridotites display olivine *J*-index (J_{Ol}) in the range 2–25 and only a few have $J_{Ol}>20$ [37].

Three main types of olivine crystallographic fabric were observed (Fig. 9):

- Orthorhombic CPO is characterized by three orthogonal point alignments of [100], [010] and [001]. Orthorhombic CPO has been measured in spinel-harzburgite (LB11), garnet-free harzburgite (LB1), dunite (LB14) and garnet-harzburgites (LB34, KAT17). Equilibrium temperatures for these samples range from 990 °C to almost 1250 °C. The fabric strength, J_{Ol}, ranges from 2.6 to 6. Clustering is usually higher for [100] than for [010] and [001]. When foliation was observed in the xenoliths, [010] is close to the pole of the foliation (*Z* structural axis). The orientation of the lineation (*X* structural axes) was determinable in sample LB9. In this sample, the main alignment of [100] is close to the observed lineation. This is the usual orientation for this very common CPO pattern [37]. For the remaining samples, the orientation of the maxima of [100] and [001] relative to the lineation remains unknown. However, since [100] is the main slip direction in olivine at high temperature (e.g., [38]), we may expect that it aligns with the lineation. CPO of harzburgite LB34 is intermediate between pure orthorhombic and [100]-fiber types (i.e., with [010] and [001] distributed in a girdle normal to the [100] maximum).
- [010]-fiber CPO [9,36] was observed in garnet-free lherzolite (LB9) and harzburgite (KAT1), and in several garnet-lherzolites (LB45, LB53, LB24) equilibrated at temperatures in the range <1100 °C to 1400 °C. The [010]-fiber CPO is characterized by a strong alignment of [010] close to the pole of the foliation and by a homogeneous distribution of [100] and [001] in a girdle that roughly parallels the foliation plane. The measured CPO is actually

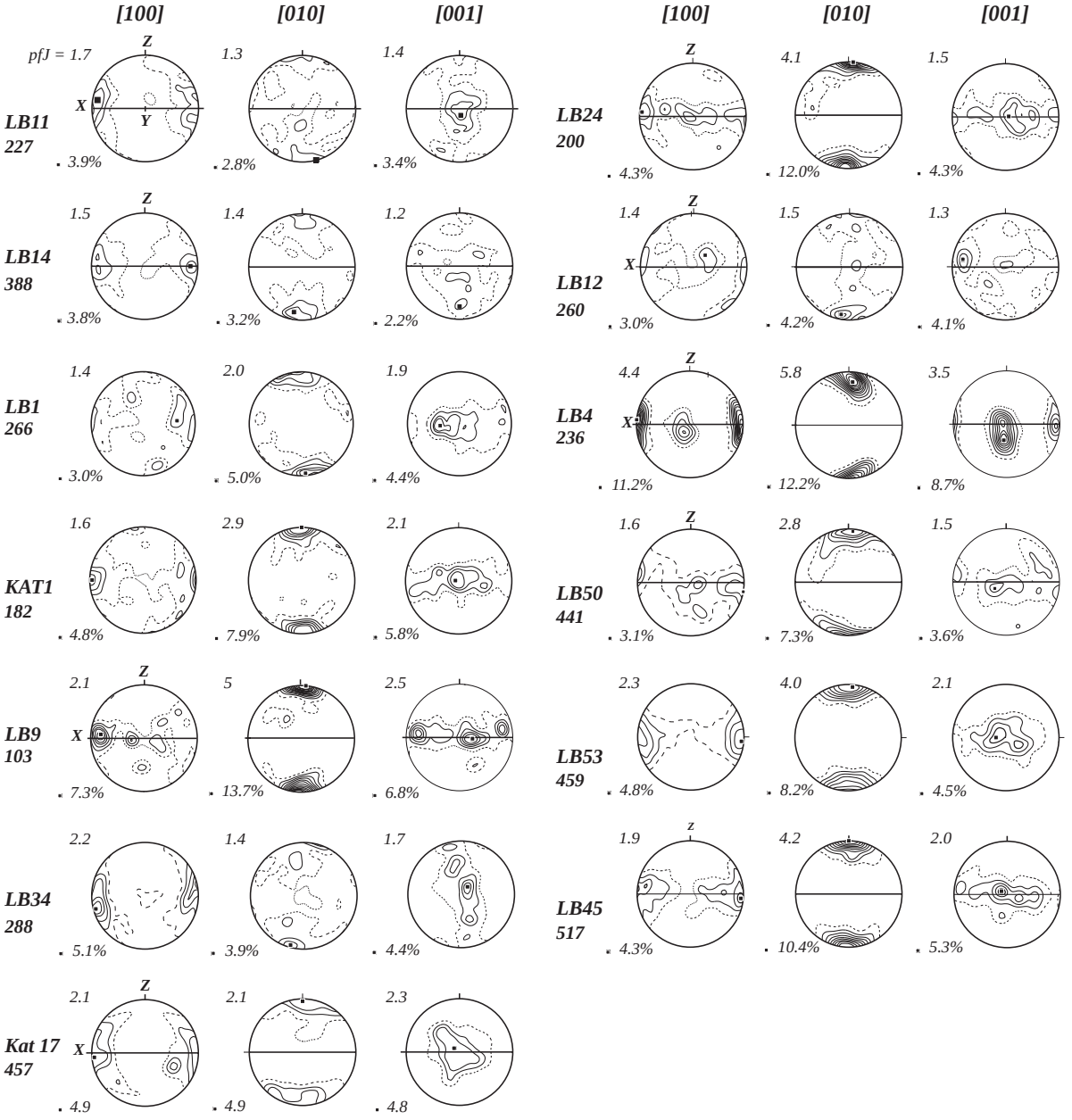

Fig. 9. Crystallographic preferred orientation of olivine. Samples are ordered from the shallowest (LB11) to the deepest (LB45). Number below the identification of the sample is number of measurements. Number below each pole figure is the maximum concentration % of the crystallographic axes; the location of the maximum is marked by a black square on the pole figure. Contours are in multiples of uniform distribution (mud). The stippled contour marks 1 mud. Foliation, when observed, is marked by a black line and the *Z* structural axis (normal to the foliation) is shown on top of the pole figure. Lineation, when determined, is marked by the structural axis *X* on the side of the pole figure. Samples for which neither the lineation nor the foliation has been determined are oriented with the maximum alignments of [100] and [010] to the left side and to the top of the pole figure, respectively. Lower hemisphere projection.

intermediate between the orthorhombic and the true [010]-fiber CPO type since the distribution within the girdles is not homogeneous. The olivine fabric strength is rather high, ranging from $J_{OI} \approx 7$ to $J_{OI} \approx 13$. These high J_{OI} values result mainly from the strong alignment of [010] close to the foliation pole.

– Bimodal CPO: The third, less common, type of CPO was observed in largely recrystallized garnet-harzburgites (LB12, LB4, LB50) equilibrated at high temperature and pressure (1269 °C–4.4 GPa to 1359 °C–4.6 GPa). It is characterized by a strong alignment of [010] close to the pole of the foliation and by a bimodal alignment of both [100] and [001] axes within the foliation. Moreover, each alignment of [100] coincides with an alignment of [001]. When the structural framework was recognized (LB12), one of the alignments of [100] and [001] is close to the *X*-axis whereas a subsidiary clustering of [100] and [001] occurs close to the *Y*-axis. This CPO was previously described in high-temperature mylonitic xenoliths from the Kapvaal craton [31].

The orthorhombic CPO is regarded as indicative of dislocation creep, with (010)[100] as the dominant slip system (e.g., [38]). The interpretations of the [010]-fiber and of the bimodal CPO are less straightforward. They might indicate an increasing contribution of the (010)[001] slip system to the deformation. Indeed, in the bimodal CPO, either [100] or [001] are favorably oriented to behave as a glide direction. In LB4 and LB24, the [100] alignment is stronger than the [001] alignment, suggesting that glide on (010)[100] was dominant, but in LB12, the [001] alignment close to *X* is slightly stronger than the [100] alignment, suggesting a balanced activity of (010)[100] and (010)[001]. An increased contribution of dislocation glide in the [001] direction might be favored by the high temperature and pressure conditions prevailing during deformation. Recent experimental results [39] have shown that, under high PT conditions, the activity of the (010)[001] slip system may overcome the activity of the (010)[100] slip system.

A more precise analysis of the olivine [100], [010] and [001] pole figure symmetry was performed using the point (*P*), girdle (*G*) and random (*R*) fabric type indexes [40] calculated from the three eigenvalues (λ_1, λ_2, λ_3) of the normalized orientation matrix for each principal crystallographic axes. These three fabric indexes are automatically computed by *D*. Mainprice's code [41] using: $P=\lambda_1-\lambda_2$, $G=2(\lambda_2-\lambda_3)$ and $R=3*\lambda_3$ [40,42]. Then, the distribution of the crystallographic axes may be represented in a triangular diagram with *P*, *G* and *R* as end-members (Fig. 10). This analysis highlights the correlation of fabric evolution with depth and recrystallization. Two groups may be defined from the repartition of [100] and [010]: For [100], a few samples fall in the *G* domain, whereas the remaining samples fall in the *R* domain. Similarly, in the [010] diagram, a few samples fall in the *P* domain and the remaining samples in the *R* domain. Both groups with lower *R* contain the xenoliths sampled at greater depth (LB24, LB4, LB50, LB53, LB45), which also display the greatest recrystallization. Two exceptions should be noted: LB12, although equilibrated at 4.4 GPa and 1290 °C, displays a weak CPO and therefore plots close to the *R* end-member. On the other hand LB9, a coarse-grained, garnet-free lherzolite displays a strong [010]-fiber type CPO and plots with xenoliths equilibrated at high *P–T* conditions. The *P–T* conditions of equilibration for this sample have not been evaluated. However, the grain size (up to 1 cm) and the evidence of large grain boundary migration (bulging, poikiloblastic olivine) characterize this sample as the most annealed of the garnet-free peridotites. As a whole, eigenvalues analysis strongly supports an evolution of olivine CPO with depth, characterized by an increase of the CPO strength, by [100] repartition within a girdle and by [010] clustering close to the foliation pole.

In many samples, the number of measured crystallographic orientations of orthopyroxene and clinopyroxene was too small to estimate whether these minerals have a CPO or not. Moreover, in most clinopyroxene-bearing xenoliths, a significant proportion of clinopyroxene crystallized from percolating melt (Fig. 11) and may have only recorded the late evolution of the mantle. Samples in which statistically representative orthopyroxene crystallographic orientations have been measured display an orthopyroxene CPO that varies from weak to relatively strong (Fig. 12). Interestingly, the deepest xenoliths tend to display rather strong orthopyroxene CPO. In those samples,

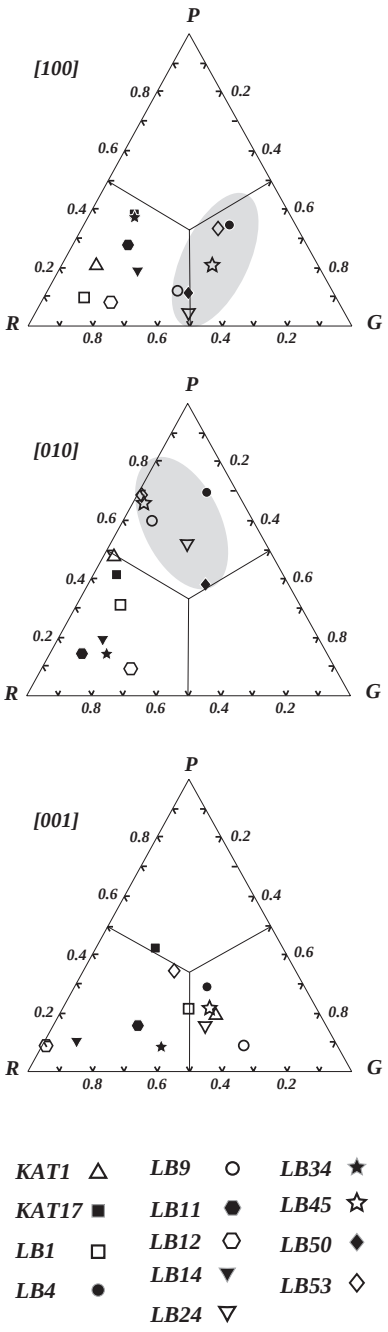

Fig. 10. Eigenvalues analysis. The olivine CPO of each sample is plotted in a triangular diagram according to the *P*, *G*, *R* indexes of the distribution of the [100], [010] and [001] crystallographic axis. Xenoliths from the deep lithosphere tend to fall either in the G domain (for [100]) or in the P domain (for [010]).

orthopyroxene [001] axes usually remain close to the [100] maximum alignment of olivine. The [100] axis of orthopyroxene tends to align with the pole of foliation, although it frequently displays a rather large dispersion. This CPO suggests deformation by dislocation creep, with dominant glide on the (100)[001] system, as is usually the case for deformed orthopyroxene in peridotites (e.g., [38]). Sample LB4, which displays a bimodal olivine CPO (Fig. 9), also shows a well-defined preferred orientation of the [001] axis of orthopyroxene (Fig. 12) that aligns close to the maximum of olivine [100] and to a subsidiary cluster of olivine [001]. This pattern suggests a major contribution of the (010)[100] and a subsidiary contribution of the (010)[001] slip systems to the deformation of olivine. In contrast, in sample LB12, the maximum alignment of orthopyroxene [001] is parallel to the maximum alignment of the olivine [001] that therefore probably represents the dominant glide direction. Sample LB45 displays a clustering of the orthopyroxene [001] located in between the maximum alignments of the olivine [100] and [001].

Both olivine and orthopyroxene CPO become stronger near the base of the cratonic lithosphere. This, together with the evidence of dislocation creep in olivine porphyroclasts, the recrystallization of olivine in relatively small grains (~500 μm) and the limited recrystallization of orthopyroxene, suggest that the lowermost cratonic lithosphere was reworked at high temperature and possibly at relatively high strain rate.

2.4. Seismic properties

The seismic properties of the Labait xenoliths have been computed by averaging the elastic constants of the individual grains in all directions, taking into account the crystallographic orientation of the main mineral phases and the modal composition of the aggregate [43]. As input parameters, we have used the crystallographic orientations of olivine, orthopyroxene and clinopyroxene (when present) presented in the previous section, the modal compositions given by Lee and Rudnick [12], the olivine, enstatite, diopside and pyrope elastic constant tensors at ambient conditions [44–47]. A Voigt–Reuss–Hill averaging was used [48]. The complete elastic tensors are shown in Table 1.

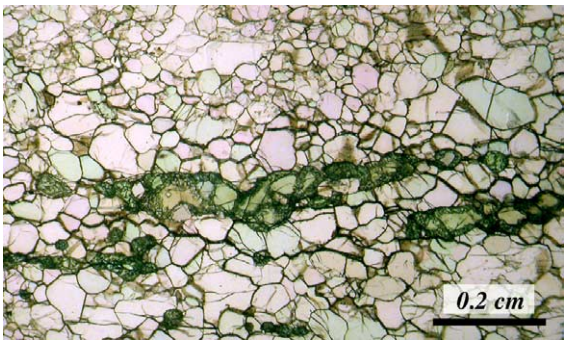

Fig. 11. Clinopyroxene veinlet in a garnet-harzburgite (KAT17). This figure suggests a refertilization of the peridotite due to melt percolation. Polarized light.

The olivine content in most mantle peridotites is high (>60%). Consequently, the seismic properties of the mantle are largely determined by olivine, and the intrinsic seismic anisotropy of mantle peridotites is mostly due to the CPO of olivine. Pyroxenes, which are also elastically anisotropic, may slightly contribute to the bulk anisotropy as far as they are preferentially oriented. The effect of orthopyroxene CPO is usually negative and tends to lower the bulk anisotropy. Random orientation of pyroxenes and the presence of garnet, which is nearly isotropic, tend to dilute the bulk anisotropy [49].

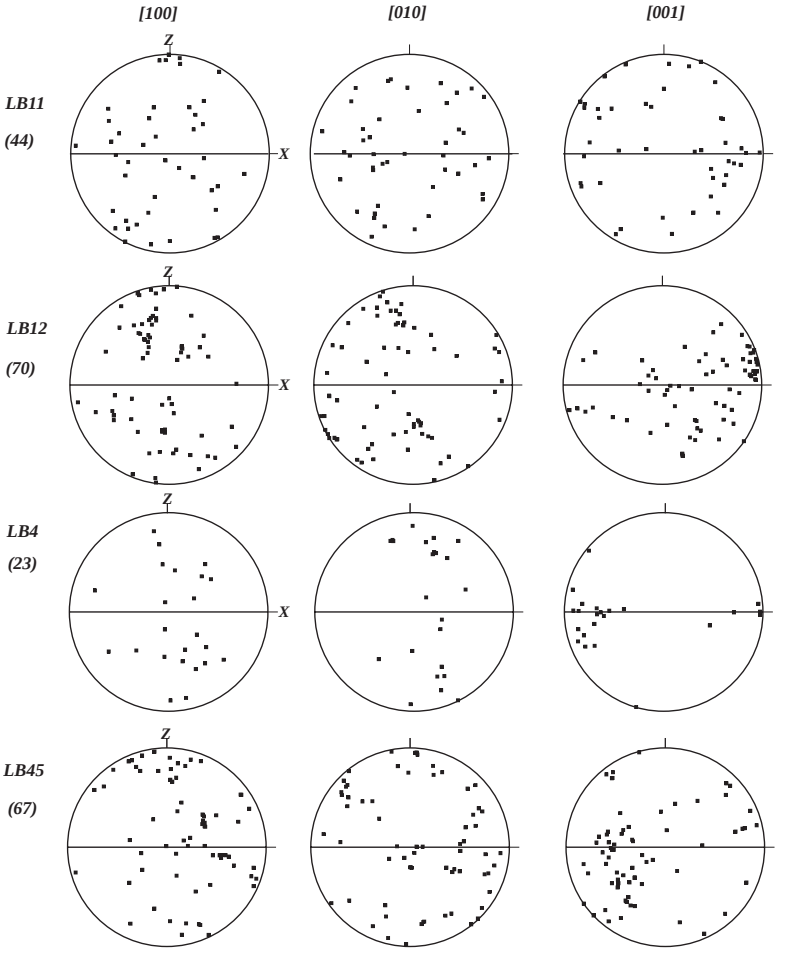

Fig. 12. Examples of orthopyroxene CPO. Pole figures as in Fig. 9 except that, due to the limited number of measurements, no density contour is shown. LB11 is the shallowest sample and displays a weak CPO. LB12 and LB4 display a clear alignment of [001] that correlates well with olivine CPO. Sample LB45, the deepest, displays a clear preferred orientation of [001] that falls in-between the clusters of olivine [100] and [001].

Table 1
Elastic constants in GPa computed using the CPO and modal composition for each sample, the elastic constants of olivine [46], enstatite [45], diopside [44] and pyrope [47] and Voigt–Reuss–Hill averaging

	C_{11}	C_{22}	C_{33}	C_{44}	C_{55}	C_{66}	C_{12}	C_{13}	C_{14}	C_{15}	C_{16}	C_{23}	C_{24}	C_{25}	C_{26}	C_{34}	C_{35}	C_{36}	C_{45}	C_{46}	C_{56}
KAT1	219.4	239.4	230.6	80.3	74.4	77.6	72.3	71.7	−0.2	−0.4	1.8	74.1	−2.3	0.7	1.3	−1.3	0.2	0.8	0.6	0.2	0.4
KAT17	215.2	243.6	217.7	78.8	72.3	79.2	69.3	71.4	−0.1	0.1	−0.3	71.0	−0.2	−0.1	0.8	−0.7	0.8	0.2	−0.3	0.0	−0.9
LB1	237.7	223.1	231.3	76.1	79.2	77.5	73.2	74.9	−0.1	0.6	0.2	73.4	0.9	0.0	−0.7	0.9	−1.1	−0.4	−0.1	−0.2	0.7
LB4	206.4	254.4	236.1	79.6	71.6	76.9	69.3	72.5	0.4	3.2	−0.6	70.1	0.2	0.5	0.0	−3.4	3.7	0.3	0.1	0.3	−1.1
LB9	239.0	211.7	231.6	74.0	80.7	75.3	71.5	71.5	0.5	−1.1	−1.0	70.8	−0.7	0.1	−0.5	−0.1	1.0	−0.6	−0.5	0.6	0.2
LB11	223.4	245.6	225.7	79.0	74.4	79.0	72.8	74.4	0.2	−1.5	−1.0	74.8	0.6	−0.1	0.0	1.2	−1.5	−0.3	0.1	−0.8	0.4
LB12	222.5	236.0	236.5	80.3	76.3	77.6	73.8	74.4	−1.2	−0.4	0.3	75.3	−3.1	−0.2	1.0	−0.6	−0.8	−0.6	−0.4	−0.3	−0.4
LB14	220.6	248.3	231.9	80.8	74.6	77.2	74.9	76.1	0.2	−0.9	−1.3	77.1	−0.6	−0.3	−1.0	0.1	−0.8	−0.3	−0.7	−1.2	0.0
LB24	225.3	220.3	238.2	75.8	79.2	76.3	72.1	72.7	0.3	−0.5	7.8	72.1	0.8	0.8	6.0	2.0	0.8	0.7	2.9	−0.5	0.1
LB34	220.8	254.8	224.7	79.3	72.9	79.9	74.6	76.5	0.1	0.6	−1.3	74.6	−0.1	0.2	−2.3	0.4	0.5	0.7	−0.3	0.8	−0.1
LB45	217.1	254.2	241.5	83.2	75.8	78.4	75.9	76.1	0.6	−1.1	−0.8	80.3	0.0	−0.3	−0.3	1.7	−1.3	0.4	0.3	0.0	−0.3
LB50	214.0	239.9	230.8	82.2	74.7	77.0	72.7	71.6	−0.1	−0.8	2.7	75.2	0,0	0.0	2.8	−1.1	−1.3	0.1	1.9	0.1	0.1
LB53	211.3	261.3	240.8	83.9	73.2	77.9	74.7	76.3	−0.2	−0.5	−0.5	79.9	−0.7	0.1	−1.3	−0.3	−0.9	−0.2	0.0	−0.3	0.1

As expected from the CPO measurements, the Labait xenoliths display a rather wide range of seismic anisotropy (Fig. 13), from 3.5 to 10.6% for Vp azimuthal anisotropy and from 2.8 to 8.3% for Vs polarization anisotropy ($AV_S\% = 100 * (V_{S_1} - V_{S_2})/(\frac{V_{S_1}+V_{S_2}}{2})$). The computed seismic properties are rather typical for mantle peridotites. Vp distribution usually displays a well-defined maximum velocity aligned with the maximum alignment of olivine [100] axes, i.e., in the X structural direction (when observed), and a minimum velocity correlated with the maximum alignment of olivine [010] axes, i.e., in the direction normal to the foliation (when observed). Slight variations of Vp distribution occur depending on the symmetry of the crystallographic axes distribution. For most samples, the seismic properties display an orthorhombic symmetry (e.g., LB14, KAT1 or LB53). In samples with a [100]-fiber type CPO, like LB34, Vp is low for waves propagating in a plane normal to the lineation (i.e., containing the Y and Z structural axes), resulting in an axial symmetry ("hexagonal" symmetry) with the lineation (maximum of [100]) as the symmetry axis. Samples with a [010]-fiber CPO (strong clustering of [010] and dispersion of [100] and [001] in a girdle parallel to the foliation) display a Vp distribution that tends towards an axial symmetry with the pole of the foliation (maximum alignment of [010]) as the symmetry axis, characterized by high velocities for P-waves propagating within or close to the foliation, and low velocities for waves propagating at high angles to the foliation.

Polarization anisotropy of samples displaying an orthorhombic CPO is characterized by a maximum birefringence (AV_S) for propagation directions close to the Y structural axis, i.e., normal to the lineation within the foliation plane. [100]-fiber CPO results in a dispersion of the high birefringence in a plane normal to $[100]_{max}$ and [010]-fiber CPO in a dispersion of the high birefringence in a plane normal to $[010]_{max}$. [100]-fiber CPO results in the minimum birefringence occurring for propagation directions close to the lineation, as is the case for mantle samples displaying an orthorhombic CPO symmetry (the most frequent in the Earth's mantle [34]). In contrast, [010]-fiber CPO results in low birefringence (or even apparent isotropy) for propagation directions at high angle to the foliation.

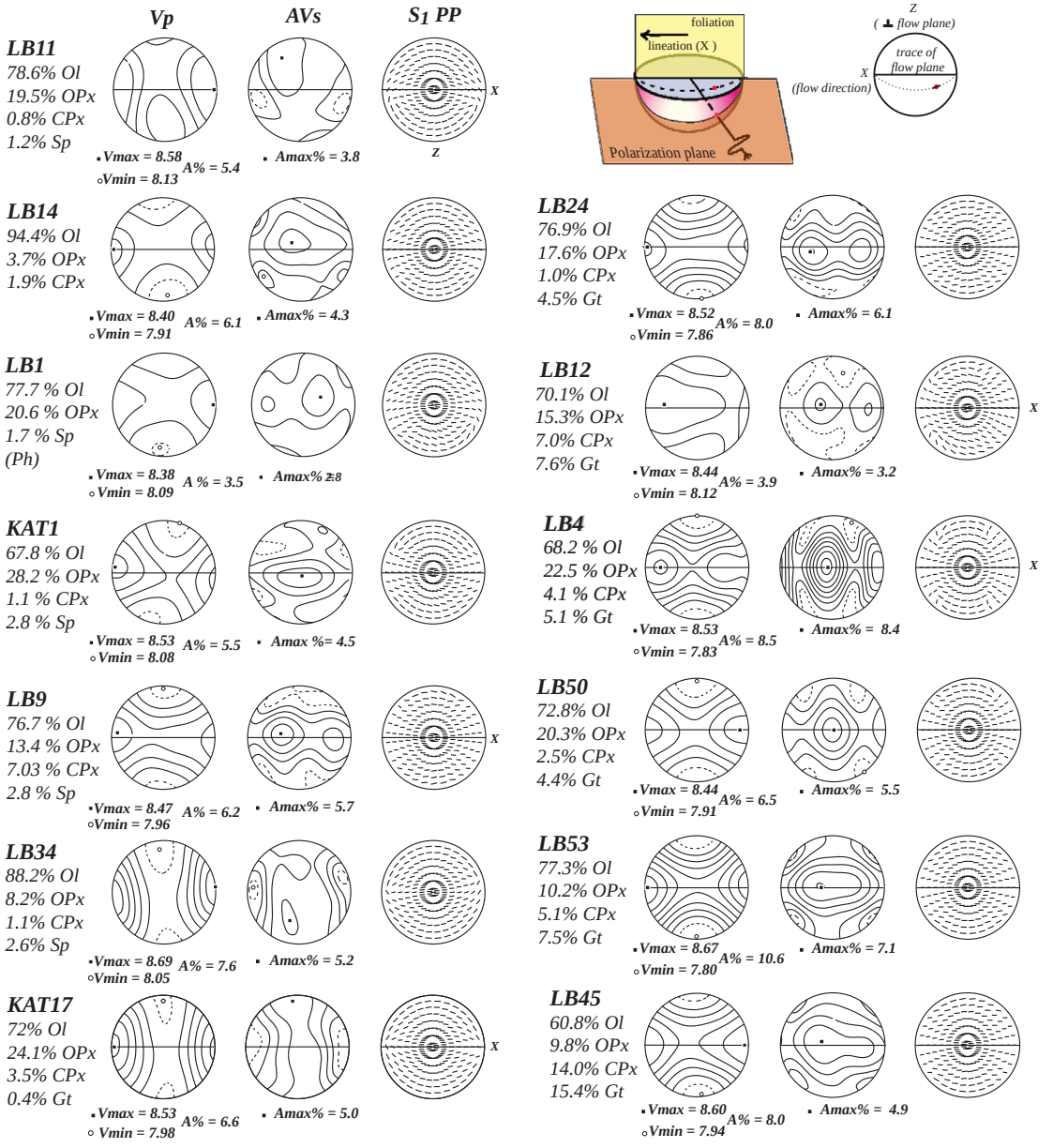

Fig. 13. Seismic properties computed from the modal composition, the crystallographic preferred orientations of olivine, orthopyroxene and clinopyroxene and the elastic properties of these minerals. For samples containing garnet, a random CPO of garnet has been used. Modal composition of each sample is given below the sample number. The first column shows the 3D variation in Vp. Black square: direction for which Vp is maximum; open circle: direction for which Vp is minimum, contours each 0.1 $km \cdot s^{-1}$. Vp_{max} and Vp_{min} are given below the diagram, as well as the maximum azimuthal anisotropy (A%). The second column shows the polarization anisotropy of S waves, contours each 1% anisotropy, the maximum birefringence is marked by a black square and the value is given below the diagram (A_{max}%). The third column shows stereographic projection of the plane in which the fast split shear wave is polarized. The great circle that results from the intersection of the polarization plane with the hemisphere is reduced to a small segment whose center corresponds to the direction of propagation of the S wave.

Independently of the CPO symmetry, the fast split shear wave (S_1) is consistently polarized in a plane containing both the propagation direction and the maximum alignment of [100] axis. It is noteworthy that even CPO with a bimodal distribution of [100] and [001] results in such polarization of the fast S wave (e.g., LB4; Fig. 13).

The least anisotropic sample is LB1, a garnet-free coarse-grained harzburgite that displays evidence of exaggerated grain growth, a weak preferred orientation of olivine [100] axes and an almost random CPO of orthopyroxene. LB53 and LB4, both equilibrated at ca. 1300 °C and 4.6 GPa (ca. 130 km deep), yield the largest anisotropy. Vp anisotropy is >10% for both samples and Vs polarization anisotropy is 7 and 9.8%, respectively. Their CPO is strong (J_{Ol}>9 for LB 53) to very strong (J_{Ol}>20 for LB4). In both samples, the CPO is characterized by a stronger clustering of olivine [010] than of [100] and [001]. Actually, the anisotropy computed for LB4 is significantly reduced by the large amount of pyroxenes and garnet (>31%). We also computed the seismic properties of both LB4 and LB53, assuming they were composed of 100% olivine. The Vp azimuthal anisotropy of the pure olivine aggregates reaches 13% for LB53 and >15% for LB4; Vs polarization anisotropy yields unusually high values: 8.6% for LB53 and 12.5% for LB4.

The influence of the garnet and pyroxene content on anisotropy is also manifested in samples LB53 and LB45 (1400 °C, 4.7 GPa) that have a very similar olivine CPO pattern and J_{Ol} (9.1 and 8.6, respectively). LB45, however, displays significantly lower azimuthal and polarization anisotropies (8.0% and 4.9%, respectively) than LB53 (10.6% and 7.0%). This difference is mostly due to the higher proportion of garnet (>15% vs. 7.5%) and clinopyroxene (14% vs. 5%) and correlated lower content of olivine (>61% vs. 77%) in LB45. On the other hand, sample LB14 has a weak CPO that yields the lowest *J*-index (J_{Ol}=2.8), but displays azimuthal and polarization anisotropies significantly higher than samples with a stronger CPO (e.g., LB1 and LB12). This is due to its dunitic composition: the anisotropy of the olivine aggregate is not diluted by the seismic properties of the other components.

3. Discussion

3.1. Microstructure and CPO of mantle rocks beneath the Labait volcano

Because the volcanism is recent, xenoliths from the Labait volcano provide important, although discontinuous, insights on the state of the cratonic mantle several million years after the mantle plume impinged on the base of the cratonic root. The vertical variation in microstructure is consistent with interaction between a mantle plume and the cratonic lithosphere. The shallowest samples, extracted from the spinel-peridotite domain, display a porphyroclastic microstructure that is rather common in the continental lithosphere [37]. This microstructure and the associated CPO may be regarded as resulting from the last significant deformation event that affected the continental lithosphere before cratonization. No evidence of subsequent heating is observed at these depths.

Xenoliths extracted from deeper levels, either the deeper gt-free-peridotites domain or the uppermost garnet-peridotite domain, display a microstructure characterized by coarse grains, absence of substructure and imbricate grain boundaries, which is likely due to significant grain-boundary mobility. This microstructure suggests that this portion of the lithosphere has been heated after deformation, enhancing diffusion and grain boundary migration. The absence of substructure indicates that heating was not followed by a deformation event in this domain. The strong CPO measured in these coarse-grained xenoliths demonstrates that enhanced diffusion and grain growth have not erased the pre-existing fabric.

The deepest samples, in the stability domain of garnet-peridotites, display evidence of nucleation recrystallization, both at grain boundaries and within grains. Two types of neoblasts are observed: “common” neoblasts that do not display a specific shape, and euhedral, “subautomorphic” neoblasts that have grown at the expense of the “common” type. Paleoclasts in recrystallized samples display subgrain boundaries suggesting that they were deformed after a grain growth episode, and that this deformation was followed by nucleation recrystallization. The magnitude of this deformation cannot be evaluated. The accumulated strain probably caused nucleation recrystallization, by generating differences in stored energy

large enough to trigger nucleation when the temperature increased, as suggested by static recrystallization experiments [34]. Collectively, these observations support a scenario in which the lower portion of the cratonic root, between 140 and 70 km, was heated by the underlying plume. This temperature increase is independently supported by petrological and geochemical data [12]. The destabilization of garnet, for instance, is regarded as resulting from a temperature rise rather than from a pressure decrease. Moreover, the downward changes in microstructure suggest that the base of the cratonic root was deformed after annealing (substructure in coarse-grained olivine) and before the onset of nucleation recrystallization (nucleation recrystallization of olivine occurs at the expense of deformed coarse paleoclasts). It is uncertain whether these three stages represent a continuous evolution or disconnected events, but given the geodynamic setting of the Labait volcano, the hypothesis of a continuous evolution is attractive. Evidence for an abnormally hot sublithospheric mantle beneath the Tanzanian craton was reported by Weeraratne et al. [3], and may represent the thermal anomaly generated by the plume head. According to Ebinger et al. [50] and Ebinger and Sleep [51], for instance, a mantle plume may have eroded the lithosphere beneath the eastern margin of the Tanzania craton during the last 40–50 My, while rifting in the Labait area may be as young as 4 My [13]. As in many other areas (e.g., [25]), rifting is therefore significantly younger than the impact of the plume. This delay may have been large enough to allow static annealing of the cratonic root, followed by deformation during rifting and recrystallization under temperature conditions favoring nucleation.

Microstructural, petrological and geochemical characteristics of the xenoliths brought to the surface by the Labait volcano suggest that the underlying lowermost lithosphere is characterized by: (1) abnormally high temperature, (2) development of a microstructure dominated by nucleation recrystallization with depth and (3) an increase in density with depth, due to greater Fe-contents of olivine. These three factors, if they combine at a sufficiently large scale, might favor a destabilization of the Archean lithosphere. Negative buoyancy may arise from density increase [12,52] and both the high temperature and active diffusion-driven nucleation recrystallization may efficiently weaken the lithospheric mantle and allow sinking of mantle blebs into the hot plume material. Such a scenario, although speculative, might represent a way by which thermo-mechanical erosion can thin the cratonic lithosphere.

3.2. Effects of recrystallization on CPO

As observed by Lee and Rudnick [12], widespread nucleation recrystallization is a characteristic of the deepest and hottest Labait xenoliths. CPO measurements show that this recrystallization does not erase the crystallographic fabric of olivine. Whether this CPO is different or largely inherited from the pre-recrystallization fabric remains difficult to assess. This is a crucial question, since CPOs of significantly different orientation in recrystallized and non-recrystallized mantle would generate variations in seismic anisotropy with depth that might perturb the anisotropy signal recorded at the surface, and could even generate an apparent isotropy. The direction of fast propagation of P-waves and the orientation of the plane in which the fastest split S-wave is polarized both depend on the orientation of the maximum alignment of the [100] olivine axes. Thus, similar CPO patterns oriented in distinct directions result in contrasting polarization characteristics. To better constrain this aspect, we measured the crystallographic orientation of neoblasts around partially recrystallized parent grains, considering that they likely represent the product of the porphyroclast recrystallization. EBSD measurements using orientation contrast imagery allow precise location of the measured grains within the thin section and thus comparison of the crystallographic orientation of neoblasts with the crystallographic orientation of neighbor paleoblasts (Fig. 14). The resulting pole figures display clusters of crystallographic axes from neighboring neoblasts. The crystallographic orientation of neoblasts surrounding a paleoclast is very similar to the orientation of the paleoclast. There is usually a weak dispersion of the neoblast crystallographic axes. Interestingly, several pole figures show clusters of neoblast crystallographic axes that do not correlate with an observed paleoclast, suggesting either that the parent grain was totally recrystallized or that it was not crosscut by the thin section. These results support the contention that nucleation recrys-

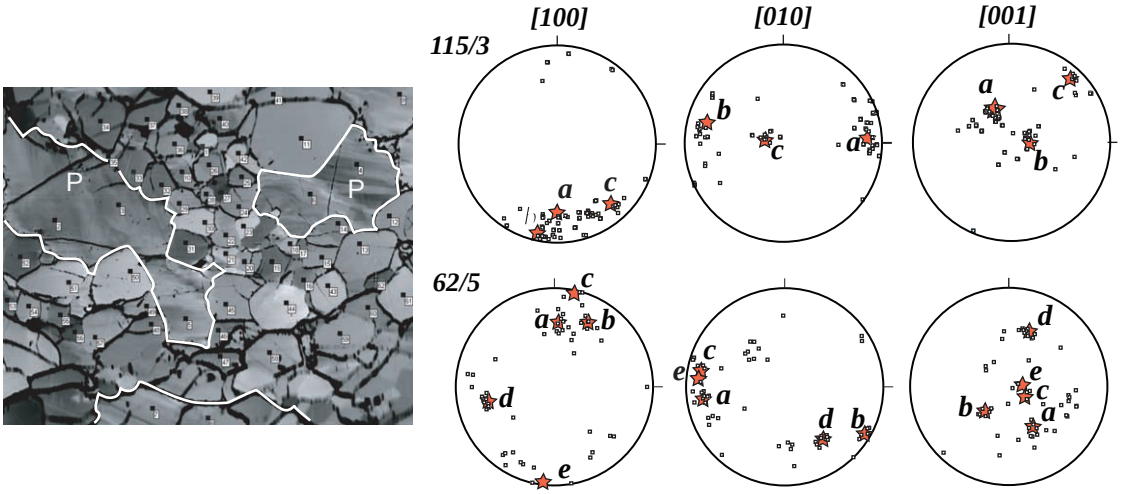

Fig. 14. Crystallographic preferred orientation of paleoclasts and surrounding neoblasts in a recrystallized garnet-harzburgite (KAT17). (A) Orientation contrast image showing paleoclasts (P) and surrounding neoblasts. The black squares are the points where a measurement has been done. The number attached to each square allows identifying measurements. (B) Pole figures of olivine crystallographic axes in two domains of the sample. Numbers on the left of the diagrams are number of neoblasts/number of paleoclasts measured for each domain. Stars and labels a–e shows the orientation of the corresponding crystallographic axis of the paleoclasts. Lower hemisphere projection. See text for discussion.

tallization in the Labait xenoliths only slightly modified the preexisting CPO and thus the related seismic anisotropy. This conclusion is only valid down to the lithosphere–asthenosphere transition. There is no evidence that coherent CPO and seismic properties exist deeper in the asthenosphere.

3.3. Seismic anisotropy

The seismic properties computed for the Labait peridotites are similar to those from both the continental and oceanic mantle lithosphere (e.g., [9,37,53,54]). Vp displays a maximum velocity parallel to the maximum alignment of olivine [100]-axis. The S-wave maximum birefringence is correlated with the *Y* structural axes and the fast split S-wave is polarized in a plane containing the propagation direction and the maximum alignment of [100] of olivine. The orientation of the polarization plane relative to the crystallographic fabric is consistent, even for samples displaying a bimodal CPO, suggesting the activation of both [100] and [001] as slip directions. The CPO variations have a larger effect on the magnitude and distribution of Vp and Vs birefringence than on the orientation of the polarization planes of S_1 and S_2. This means that the polarization of the split shear waves is only weakly sensitive to CPO variations, and remains correlated with the tectonic fabric, even when [001] of olivine is an active slip direction, as long as it is not significantly dominant over [100].

The most striking result is that anisotropy does not decrease with depth. Indeed, the opposite is true as the deepest samples display the highest anisotropies, even when they contain a large amount of garnet. For instance, the average anisotropy computed by stacking CPO measurements from LB50, LB53 and LB45 that, according to petrologic data [12], lie close to the lithosphere–asthenosphere boundary, yields 8% azimuthal anisotropy for Vp and 5.35% polarization anisotropy for Vs. These results have important implications for the seismic properties of the cratonic lithosphere: (1) the mantle beneath the Labait volcano is anisotropic, at least as deep as ~140 km; (2) thermochemical interaction (i.e., heating, recrystallization and metasomatism) of the mantle plume with the cratonic keel did not erase seismic anisotropy; (3) neither grain growth nor nucleation recrystallization erased the seismic anisotropy; rather, it appears that HT processes tend to better align the [010] axis, resulting in enhanced anisotropy; (4) sample LB45, which has asthenospheric chemical characteristics

[12], is as anisotropic as samples from the lower cratonic lithosphere.

Our conclusions are consistent with and complement those already obtained from the Ronda (Southern Spain) peridotite massif [9] and xenoliths from French Polynesia [54]. Vauchez and Garrido [9] studied the evolution of the microstructure, crystallographic fabric and seismic properties of spinel-peridotites across a partial-melting boundary believed to mark the limit between the unaffected lithosphere and the asthenospherized mantle. They concluded that propagation of a partial-melting front across the lithosphere, although it modifies the microstructure, does not erase the pre-existing CPO and related seismic anisotropy. Tommasi et al. [54] reached similar conclusions from their study of xenoliths from various islands of the French Polynesia archipelago. They showed that increasing interaction with plume-related melts results in significant Fe-enrichment of the peridotites, but it does not modify seismic anisotropy. Dispersion of olivine CPO and hence dilution of the anisotropy was only observed in dunites and wehrlites, which probably represent limited zones of enhanced melt percolation or accumulation.

In order to use our observations to interpret seismic data, we need to address the extent to which the structural and crystallographic fabrics we observed are vertically coherent and whether our observations hold at a scale pertinent for seismological observation. To do this would require knowing the orientation of the xenoliths before extraction, which is of course not possible. It is, however, possible to gain some insight from seismological observations. Weeraratne et al. [3], attempted to model the radial anisotropy expected from a plume that impacted the base of the Tanzanian cratonic lithosphere. Using Raleigh wave azimuthal anisotropy, they found that limiting anisotropy to the asthenosphere provides less reliable solutions than considering a coherent anisotropy over most of the mantle lithosphere. They even suggested that their results would be better explained by assuming that the mantle is anisotropic up to the Moho. These results, together with our own measurements, favor a coherent fabric and seismic anisotropy over the lithospheric, and part of the asthenospheric mantle.

Using the seismic properties computed for the xenoliths, one can estimate the magnitude of shear wave splitting of a vertically incident teleseismic shear wave beneath the Labait volcano. Such estimates strongly depend on the orientation of the foliation at depth, on the strength of the CPO and on the dominant symmetry of the seismic properties. Although the first is unknown, the latter two have been determined in this study and thus we can use limiting cases for the orientation of the foliation in order to obtain estimates of the magnitude of shear-wave splitting that can be generated in the mantle lithosphere. For instance, olivine CPO with a [010]-fiber symmetry results in polarization anisotropy characterized by a low S-wave birefringence in a direction normal to the foliation, and significantly larger birefringence for directions close to the foliation. On the other hand, [100]-fiber CPO results in large birefringence for directions normal to the lineation. In this case, S-waves propagating in a direction normal to the foliation would record a rather large splitting. Assuming that our data set is representative of the lithospheric section, on average, S-wave birefringence in a direction normal to the foliation is low, around 2%. A consistently flat foliation over the entire lithospheric mantle thickness (100–110 km) would result in a delay time of <0.5 s and a transverse-isotrope symmetry. Even if an additional few tenths of second were generated within the crust, the total splitting would remain significantly less than 1 s. The maximum birefringence in our data set is consistently in a direction normal to the lineation within the foliation (normal to the maximum alignment of both [100] and [010]), which is typical of naturally deformed peridotites [37]. On average, the birefringence in this direction is 5–6%. Assuming a steeply dipping foliation and a subhorizontal lineation (maximum alignment of olivine [100]), the delay time between the fast and slow split waves, for a vertically incident S-wave, would be ≥ 1 s, to which the contribution from the crust, if any, should be added. In addition, in both cases (flat or steeply dipping foliation), the fast split S-wave would be polarized in a plane containing the maximum alignment of olivine [100].

The above estimates can be compared with splitting measurements obtained by Walker et al. [24] in East Africa. Splitting parameters were retrieved from two stations located close to the Labait volcano (BASO and KOND). At BASO, the polar-

ization of the fast S-wave is consistently NNW to NS and the delay time varies around 1 s (±0.3 s). At KOND, two directions of polarization have been found, close to NS (parallel to the rift) and NW–SE (parallel to tectonic structures in the craton. Delay time at KOND is systematically higher than 1 s. Considering the seismic properties estimated from the Labait xenoliths, splitting parameters at BASO may be accounted for by an anisotropic lithosphere with a steeply dipping foliation and a ~NS lineation. Interpretation of fast S-wave polarization at KOND is less straightforward, since two orientations have been found. Both might be explained by a lithospheric fabric, but their coexistence is still poorly understood. Delay time at KOND can be explained by a lithospheric source only if the lithosphere is 20 to 50 km thicker than under the Labait volcano, or if significant anisotropy (parallel to that in the mantle) exists in the crust. Otherwise, a contribution from the sublithospheric mantle or from aligned melt pockets is needed. A lithospheric source of anisotropy is likely for stations located within the Mozambique belt away from the rifted domain (HALE, KIBE, KIBA, [24]) where the fast S-wave polarization is consistently parallel to the orogenic grain of the Mozambique belt. This suggests that the East African Rift developed along pre-existing Neoproterozoic lithospheric fabric [25]. In a rifted domain, other sources of anisotropy may contribute to the observed splitting (e.g., [55]). A contribution from aligned melt pockets or of asthenospheric flow below the rifted lithosphere is possible. Melt pocket alignment is favored to explain anisotropy further north, in Ethiopia [23], and flow at the base of the lithosphere is suggested for some stations in Kenya and Tanzania [24]. The magnitude of the delay time at BASO and KOND, the consistency of fast S-wave polarization at BASO and the relative lack of success of two-layers models [24] suggest that these various sources, if present, combine positively.

4. Conclusions

Combining microstructure and CPO measurements with petrological and geochemical data strongly suggests that melt percolation, reheating and nucleation recrystallization related to impingement of a mantle plume at the base of the cratonic Tanzanian lithosphere did not erase the CPO of mantle minerals. The cratonic lithosphere beneath the Labait volcano is thus seismically anisotropic down to the lithosphere–asthenosphere boundary at ~140 km. The transition between the lithosphere and the asthenosphere seems to be progressive from a microstructural and textural point of view. This domain was likely deformed after a period of static annealing and grain growth. This deformation might be related to the plume dynamics. Shear-wave splitting measurements performed at stations close to the Labait volcano [24] may be accounted for by a lithospheric anisotropy corresponding to our estimates, assuming a steeply dipping foliation and a shallowly plunging lineation. Nonetheless, contributions from other sources of anisotropy cannot be rule out as far as their effect combines positively with the mantle lithospheric anisotropy.

These results are consistent with Vauchez and Garrido's [9] suggestion that a "ghost", transitional lithosphere may develop above a mantle plume. This domain displays "asthenospheric" seismic velocities (a few % negative anomaly relative to PREM) and "lithospheric" seismic anisotropies. A similar model is valid beneath the Labait domain: both the thermal anomaly and the Fe-enrichment of olivine would produce a negative seismic velocity anomaly [52]. Plume–lithosphere interaction, although it triggers crystal growth, does not erase the initial CPO and seismic anisotropy; even at great depths, where nucleation recrystallization becomes widespread, the CPO of neoblasts is largely inherited from the original crystals. These conclusions also are in good agreement with the Nyblade et al. [10] body-wave tomographic model, which suggests the presence of a thick domain of perturbed lithosphere up to a depth of ca. 100 km. Our results suggest that this domain is likely to have preserved an inherited "lithospheric" anisotropy.

Acknowledgements

This work benefited greatly from David Mainprice's codes, developed to process EBSD orientation measurements and to calculate seismic properties from CPO. Christophe Nevado and Doriane Delmas prepared the high quality polished thin sections needed for EBSD measurements. We are indebted to

Mike Kendall, Geoff Lloyd and Andrea Tommasi for helpful criticism and suggestions.

References

[1] T.H. Jordan, Composition and development of the continental lithosphere, Nature 274 (1978) 544–548.
[2] J. Ritsema, A.A. Nyblade, T.J. Owens, C.A. Langston, J.C. VanDecar, Upper mantle seismic velocity structure beneath Tanzania, East Africa; implications for the stability of cratonic lithosphere, J. Geophys. Res. 103 (1998) 21201–221213.
[3] D.S. Weeraratne, D.W. Forsyth, K.M. Fischer, Evidence for an upper mantle plume beneath the Tanzania craton from Rayleigh wave tomography, J. Geophys. Res. 108 (2003), doi:10.1029/2002JB00273.
[4] M.A. Menzies, J.-L. Bodinier, Growth of the European lithospheric mantle; dependence of upper-mantle peridotite facies and chemical heterogeneity on tectonics and age, Phys. Earth Planet. Inter. 79 (1993) 219–240.
[5] R.L. Rudnick, W.F. McDonough, R.J. O'Connell, Thermal structure, thickness and composition of continental lithosphere, Chem. Geol. 145 (1998) 395–411.
[6] M.-P. Doin, L. Fleitout, U. Christensen, Mantle convection and stability of depleted and undepleted continental lithosphere, J. Geophys. Res. 102 (1997) 2771–2787.
[7] A. Lenardic, L. Moresi, H. Muehlhaus, The role of mobile belts for the longevity of deep cratonic lithosphere; the crumple zone model, Geophys. Res. Lett. 27 (2000) 1235–1238.
[8] C. Morency, M.-P. Doin, C. Dumoulin, Convective destabilization of a thickened continental lithosphere, Earth Planet. Sci. Lett. 202 (2002) 303–320.
[9] A. Vauchez, C.J. Garrido, Seismic properties of an asthenospherized lithospheric mantle: constraints from lattice preferred orientations in peridotite from the Ronda Massif, Earth Planet. Sci. Lett. 192 (2001) 235–249.
[10] A.A. Nyblade, T.J. Owens, H. Gurrola, J. Ritsema, C.A. Langston, Seismic evidence for a deep upper mantle thermal anomaly beneath East Africa, Geology 28 (2000) 599–602.
[11] J. Ritsema, S. Ni, D.V. Helmberger, H.P. Crotwell, Evidence for strong shear velocity reductions and velocity gradients in the lower mantle beneath Africa, Geophys. Res. Lett. 25 (1999) 4225–4228.
[12] C.T. Lee, R.L. Rudnick, Compositionally stratified cratonic lithosphere; petrology and geochemistry of peridotite xenoliths from the Labait Volcano, Tanzania, Proceedings of the International Kimberlite Conference 7, vol. 2, 1999, pp. 503–521.
[13] J.B. Dawson, Neogene tectonics and volcanicity in the North Tanzania sector of the Gregory Rift valley; contrasts with the Kenya sector, Tectonophysics 204 (1992) 81–92.
[14] J.B. Dawson, Quaternary kimberlitic volcanism on the Tanzania Craton, Contrib. Mineral. Petrol. 116 (1994) 473–485.
[15] J. Ritsema, H.-J. van Heijst, J.H. Woodhouse, Complex shear wave velocity structure imaged beneath Africa and Iceland, Science 286 (1999) 1925–1928.
[16] N. Rogers, R. Macdonald, G. Fitton, R. George, M. Smith, B. Barreiro, Two mantle plumes beneath the East African rift system: Sr, Nd an Pb isotope evidence from Kenya Rift basalts, Earth Planet. Sci. Lett. 176 (2000) 387–400.
[17] A.A. Nyblade, C.A. Langston, T.J. Owens, H. Gurrola, J. Ritsema, S.D. Malone, Evidence for a mantle plume in East Africa from the Tanzania broadband seismic experiment, Seismol. Res. Lett. 70 (1999) 261.
[18] J. Ritsema, H.-J. van Heijst, New seismic model of the upper mantle beneath Africa, Geology 28 (2000) 63–66.
[19] K. Theunissen, J. Klerkx, A. Melnikov, A. Mruma, Mechanisms of inheritance of rift faulting in the western branch of the East African Rift, Tanzania, Tectonics 15 (1996) 776–790.
[20] A. Vauchez, G. Barruol, A. Tommasi, Why do continents break up parallel to ancient orogenic belts? Terra Nova 9 (1997) 62–66.
[21] S. Gao, P.M. Davis, H. Liu, P.D. Slack, W. Rigor, Y.A. Zorin, V.V. Mordvinova, V.M. Kozhevnikov, N.A. Logatchev, SKS splitting beneath continental rift zones, J. Geophys. Res. 102 (1997) 22781–22797.
[22] G. Barruol, W. Ben Ismail, Upper mantle anisotropy beneath the African IRIS and Geoscope stations, Geophys. J. Int. 146 (2001) 549–561.
[23] J.-M. Kendall, G.W. Stuart, C.J. Ebinger, I.D. Bastow, D. Keir, Magma-assisted rifting in Ethiopia, Nature 3161 (2004), doi:10.1038/nature03161.
[24] K.T. Walker, A.A. Nyblade, S.L. Klemperer, G. Bokelmann, T.J. Owens, On the relationship between extension and anisotropy: constraints from shear wave splitting across the East African Plateau, J. Geophys. Res. 109 (2004), doi:10.1029/2003JB002866.
[25] A. Tommasi, A. Vauchez, Continental rifting parallel to ancient collisional belts: an effect of the mechanical anisotropy of the lithospheric mantle, Earth Planet. Sci. Lett. 185 (2001) 199–210.
[26] J.T. Chesley, R.L. Rudnick, C.-T. Lee, Re–Os systematics of mantle xenoliths from the East African Rift; age, structure, and history of the Tanzanian Craton, Geochim. Cosmochim. Acta 63 (1999) 1203–1217.
[27] G.P. Brey, T. Koehler, Geothermobarometry in four-phase lherzolites: II. New thermobarometers, and practical assessment of existing thermobarometers, J. Petrol. 31 (1990) 1353–1378.
[28] A.A. Nyblade, Heat flow and the structure of Precambrian lithosphere, Lithos 48 (1999) 81–91.
[29] R.L. Rudnick, A.A. Nyblade, The thickness and heat production of Archean lithosphere; constraints from xenolith thermobarometry and surface heat flow, Spec. Publ. - Geochem. Soc. 6 (1999) 3–12.
[30] J.B. Dawson, D. James, C. Paslick, A.M. Halliday, Ultrabasic potassic low-volume magmatism and continental rifting in north-central Tanzania; association with enhanced heat flow, Russ. Geol. Geophys. 38 (1997) 69–81.
[31] A.M. Boullier, A. Nicolas, Classification of textures and fabrics of peridotites xenoliths from South African kimberlites, Phys. Chem. Earth 9 (1975) 467–475.

[32] J.-C. Mercier, Peridotites xenoliths and the dynamic of kimberlite intrusion, in: F.R. Boyd, H.O.A. Meyer (Eds.), The Mantle Sample, Inclusions in Kimberlites and Other Volcanics, vol. 2, American Geophysical Union, Washington, 1979, pp. 197–212.
[33] J.-C. Mercier, A. Nicolas, Textures and fabrics of upper mantle peridotites as illustrated by xenoliths from basalts, J. Petrol. 16 (1975) 454–487.
[34] S. Nermond, Etude expérimentale de la recristallisation statique et de la cinétique de croissance de l'olivine, PhD, Université de Paris VII, 1994.
[35] M.R. Drury, H.M.L. Van Roermund, Fluid-assisted recrystallization in upper mantle peridotite xenoliths from kimberlites, J. Petrol. 30 (1989) 133–152.
[36] H.J. Bunge, Texture Analysis in Materials Sciences, Buttleworth, London, 1982, 593 pp.
[37] W. Ben Ismaïl, D. Mainprice, An olivine fabric database: an overview of upper mantle fabrics and seismic anisotropy, Tectonophysics 296 (1998) 145–158.
[38] A. Nicolas, J.P. Poirier, Crystalline Plasticity and Solid State Flow in Metamorphic Rocks, Wiley, London, 1976, 444 pp.
[39] H. Couvy, D. Frost, F. Heidelbach, K. Nyilas, T. Ungár, S. Mackwell, P. Cordier, Shear deformation experiments of forsterite at 11 GPa–1400 °C in the multianvil apparatus., Eur. J. Mineral. (in press).
[40] F.W. Vollmer, An application of eigenvalue methods to structural domain analysis, Geol. Soc. Am. Bull. 102 (1990) 786–791.
[41] S. Ulrich, D. Mainprice, Does cation ordering in omphacite influence development of lattice-preferred orientation? J. Struct. Geol. (in press).
[42] A. Mauler, G. Godard, K. Kunze, Crystallographic fabrics of omphacite, rutile and quartz in Vendée eclogites (Armorican Massif, France). Consequences for deformation mechanisms and regimes, Tectonophysics 342 (2001) 80–112.
[43] D. Mainprice, M. Humbert, Methods of calculating petrophysical properties from lattice preferred orientation data, Surv. Geophys. 15 (1994) 575–592.
[44] M.D. Collins, J.M. Brown, Elasticity of an upper mantle clinopyroxene, Phys. Chem. Miner. 26 (1998) 7–13.
[45] T.S. Duffy, M.T. Vaughan, Elasticity of enstatite and its relationships to crystal structure, J. Geophys. Res. 93 (1988) 383–391.
[46] E.H. Abramson, M. Brown, L.J. Slutsky, J. Zaug, The elastic constants of San Carlos olivine up to 17 GPa, J. Geophys. Res. 102 (1997) 12252–212263.
[47] M. Chai, J.M. Brown, L.J. Slutsky, The elastic constants of a pyrope-grossular-almandine garnet to 20 GPa, Geophys. Res. Lett. 24 (1997) 523–526.
[48] R. Hill, The elastic behavior of a crystalline aggregates, Proc. R. Soc. Lond., A 65 (1952) 349–354.
[49] D. Mainprice, G. Barruol, W. Ben Ismaïl, The seismic anisotropy of the Earth's mantle: from single crystal to polycrystal, in: S.-I. Karato, A.M. Forte, R.C. Liebermann, G. Masters, L. Stixrude (Eds.), Earth's Deep Interior: Mineral Physics and Seismic Tomography: From Atomic to Global, AGU Geophysics Monograph, vol. 117, 2000, pp. 237–264.
[50] C. Ebinger, Y. Pojom-Djomany, E. Mbede, A. Foster, J.B. Dawson, Rifting Arcaean lithosphere: the Eyasi-Manyara-Natron rifts, East Africa, J. Geol. Soc. (Lond.) 154 (1997) 947–960.
[51] C. Ebinger, N. Sleep, Cenozoic magmatism throughout east Africa resulting from impact of one large mantle plume, Nature 395 (1998) 788–791.
[52] C.-T.A. Lee, Compositional variation of density and seismic velocities in natural peridotites at STP conditions: implications for seismic imaging of compositional heterogeneities in the upper mantle, J. Geophys. Res. 108 (2003) 2441, doi:10.1029/2003JB002413.
[53] H. Kern, L. Burlini, I.V. Ashchepkov, Fabric-related seismic anisotropy in upper-mantle xenoliths: evidence from measurements and calculations, Phys. Earth Planet. Inter. 95 (1996) 195–209.
[54] A. Tommasi, M. Godard, G. Coromina, J.M. Dautria, H. Barczus, Widespread melt/rock interaction and seismic properties of the lithospheric mantle above plumes: a petrological and microstructural study of mantle xenoliths from French Polynesia., Earth Planet. Sci. Lett. 227 (2004) 539–556.
[55] A. Vauchez, A. Tommasi, G. Barruol, J. Maumus, Upper mantle deformation and seismic anisotropy in continental rifts, Phys. Chem. Earth 25 (2000) 111–117.